Electroweak corrections to Higgs boson production via Z Z fusion at the future LHeC

Hanying Xiong,[*] Hongsheng Hou,[†] Zhuoni Qian,[‡] Qingjun Xu,[§] and Bowen Wang[‖]
School of Physics, Hangzhou Normal University, Hangzhou, Zhejiang 311121, China

(Received 4 December 2023; accepted 20 May 2024; published 24 June 2024; corrected 29 July 2024)

An important mechanism for production of the Higgs boson at the prospective Large Hadron-electron Collider (LHeC) is via neutral current (NC) weak boson fusion (WBF) processes. Aside from its role in measurements of Higgs couplings within the standard model, this production mode is particularly useful in searchings of Higgs decays into invisible particles in various models for the Higg portal dark matter. In this work we compute the electroweak corrections for the NC WBF at the LHeC up to the one-loop level. For a center-of-mass energy of 1.98 TeV, the magnitudes of the relative corrections for the total cross section at next-to-leading (NLO) order are respectively 8% and 17%, in the two renormalization schemes we use. The NLO terms also distort various distributions (notably, those for Higgs and electron observables) computed at the leading order. Along with our previous treatment of the charge current processes, this paper completes the calculation of the NLO electroweak effects for the dominant Higgs production modes at the LHeC.

DOI: 10.1103/PhysRevD.109.116021

I. INTRODUCTION

Various Higgs boson production mechanisms have been explored to study the properties of the particle, especially over the decade after its discovery [1,2]. Among these, the production of the Higgs via weak boson fusion (WBF) has unique kinematic characteristics that have been successfully utilized in the determination of Higgs couplings with other particles. For instance, the measurement of Higgs-gauge boson couplings was found to be sensitive to the WBF production mode (as well as to other modes such as the gluon-gluon fusion (ggH) at the LHC [3,4]. The combined analysis reaches an accuracy at the percent level. In addition, this channel also plays an important role in probing the $H \to \tau^+\tau^-$ decay [5,6].

To avoid large QCD background, the measurement of Higgs-Yukawa couplings with light quarks is proposed to be performed at lepton-hadron colliders such as the future LHeC [7],[1] which is planned to run at a center-of-mass energy of 1–2 TeV with the current proton beam at the LHC scattering on an additional beam of electrons. Studies have already shown the potential of probing the H-b Yukawa coupling at the LHeC [7–9], where Higgs bosons are predominantly produced via WBF. Positive results are also obtained in restricting the H-c Yukawa and triple-Higgs-self couplings [9–11]. These advancements give rise to the need for including higher-order corrections of the cross sections in the simulations of the relevant processes. In fact, the QCD [12] and part of the electroweak [13] corrections to the Higgs WBF production on ep colliders at one-loop level were computed even before many of these phenomenological studies.

In a previous paper [14], we[2] treated the Higgs WBF production via W boson fusion with the full electroweak (EW) corrections at one-loop [next-to-leading order (NLO)]. At the tree level, the charge current (CC) processes account for approximately 80% of the total cross section for Higgs production at the energy regime of the LHeC. However, the neutral current (NC) processes via Z Z fusion is not negligible, and moreover, has its own merit because the final state electrons can be observed in about half of the NC WBF events (in contrast to the missing energy carried by neutrinos in CC events). The NC final state will typically contain two visible fermions with large rapidity difference

[*]21736003@zju.edu.cn
[†]hshou@hznu.edu.cn
[‡]sdaly@126.com
[§]xuqingjun@hznu.edu.cn
[‖]Contact author: bowenw@hznu.edu.cn

Published by the American Physical Society under the terms of the Creative Commons Attribution 4.0 International license. Further distribution of this work must maintain attribution to the author(s) and the published article's title, journal citation, and DOI. Funded by SCOAP[3].

[1]Of course, there are many other motivations for building the LHeC. For more details see e.g., Ref. [7].

[2]Two of the three authors of this reference are in the author list of the current paper.

and invariant mass, as well as the products from the fusion subprocesses near the central region of the rapidity gap. This configuration not only provides a prospect of restricting the H-b coupling with the NC WBF [8], but is also useful particularly when probing final states with invisible fusion products, thanks to the kinematic handles provided by the forward and backward fermions.[3]

In fact, studies at the LHC are the first to make use of the WBF mode in dark matter searches [15–19], where the forward and backward jets can be tagged in both CC and NC processes. In particular, Higgs decays to dark matter particles allowed by various extensions [20–27] of the standard model (SM) are investigated experimentally by ATLAS [28] and CMS [29] groups. In these searches, the ggH mode with jets is not preferable since it suffers from large background, e.g., $Z \to \nu\bar{\nu} +$ jets in the central region. Due to lack of discriminative power from the event topology, strict restrictions on the jets have to be imposed in order to suppress the background, which substantially lowers the signal rate. The search in VH (V denotes W or Z) production, where V decays leptonically, gives better result, but WBF turns out to be the most sensitive channel in identifying invisible decays of the Higgs, and sets the lowest upper limit (18% by CMS [30,31] and 28% by ATLAS [32,33], at 95% confidence level) for the branching ratio of these decays.

On the other hand, it is shown that more stringent limit is to be expected at the LHeC, where the background involves Z and W bosons produced via purely EW interactions [34]. In contrast, the background for the LHC analysis includes $\mathrm{Z/W} +$ jets, with jets produced by strong interactions, which is less clean and controllable. However, the WW fusion processes cannot be used in dark matter searches at the LHeC as the single jet signal is not quite differentiable from the charge current deep inelastic scattering. The study in Ref. [34] focuses then on the NC processes and reaches an upper limit of 6% at 2σ level.

Encouraged by these results, we are to carry out in this paper the calculation of the EW corrections for the NC WBF processes at the LHeC. As a sequel work of Ref. [14], we shall follow closely the method and notations of our previous treatment of the CC processes, and organize the rest of this paper as follows. Section II gives the details of the calculation. Section III shows numerically the significance of the NLO corrections for the NC processes. In Sec. IV we discuss the result and conclude the paper.

II. CALCULATION OF THE PROCESSES

In describing the treatment of the NC processes, we shall keep to the minimum the discussion that repeats the CC calculation [14], and focus more on the new features of the NC processes.

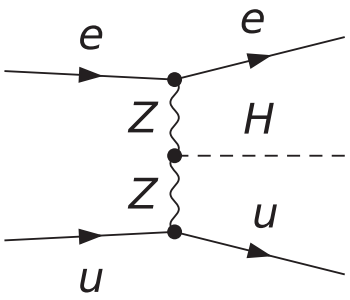

FIG. 1. The LO graph with an incoming u quark for NC WBF at the LHeC.

A. Leading-order contribution

The leading-order (LO) cross section for the NC processes is computed according to

$$\sigma^{\mathrm{LO}} = \sum_q \int_0^1 d\eta_q f_q(\eta_q, \mu_F) \frac{1}{2\hat{s}} d\Phi_3 B(P_A, p_q), \quad (1)$$

where the squared amplitude $B(P_A, p_q)$ for the born process $eq \to eqH$, along with the corresponding flux factor, is convolved with the proper parton distribution function. The result is then summed over all quark (antiquark) flavors, except for t, and $\bar{t}$, whose contributions are marginal. The LO graph with one quark flavor is shown in Fig. 1.

B. NLO EW corrections

The calculation of NLO EW corrections involves cancellation of various types of singularities and must be treated with care. As with the CC case, here we still work in the framework of the dipole subtraction method [35,36], and organize the calculation into numerical integrations over 4- and 3-particle final states, respectively.

1. 4-particle final states

Neglecting the contribution from t, b, and their antiparticles[4] gives 52 NLO real emission graphs with a photon in the initial or final state[5] (see graphs with one quark flavor in Fig. 2). These graphs, as well as the LO ones, are evaluated with the packages FeynArts, FormCalc, and LOOPTOOLS [37,38]. The photon induced graphs may involve resonant propagators and are handled with the complex-mass-scheme [39–41] in the calculation.

The subtraction term of the real emission processes has the form,

[3]The classification into "forward", "backward", and "central" may be changed by boosts along the beams, but it is possible to distinguish various final states with observables such as the rapidities of the particles.

[4]The contribution from b and $\bar{b}$ distributions at NLO (in both real and virtual emission processes) is at the level of 0.5% and is dropped in this calculation.

[5]The masses of the quarks and the electron are set to zero so that the number of contributing graphs is largely reduced.

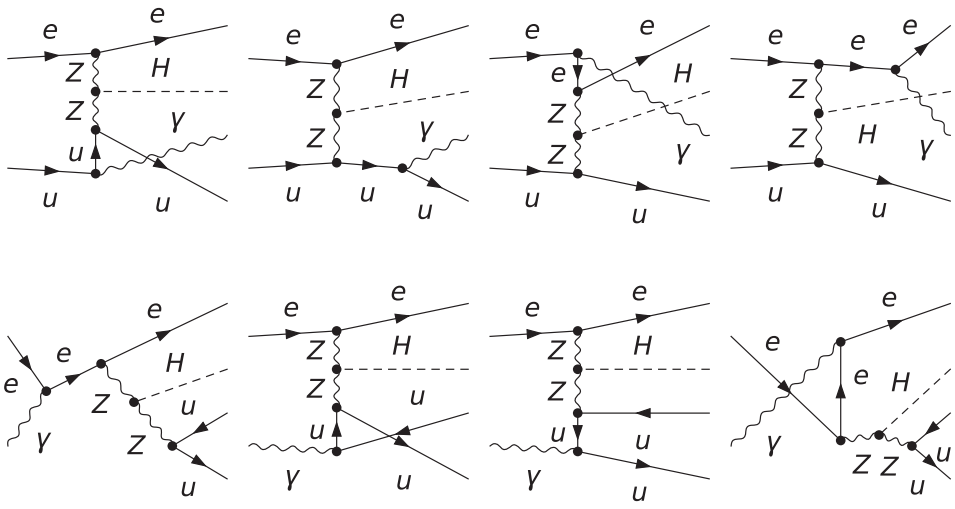

FIG. 2. Real-emission graphs with one quark flavor for NC WBF at the LHeC. The first and second lines correspond respectively to the processes $e^- + q \to e^- + \gamma + q + H$ and $e^- + \gamma \to e^- + q + \bar{q} + H$, in which $q = u$.

$$|\mathcal{M}_{\rm sub}|^2 = \sum_{i,j}\sum_{k}\mathcal{D}_{ij,k} + \sum_{i,j}\sum_{a}\mathcal{D}^a_{ij} + \sum_{a,j}\sum_{k\neq j}\mathcal{D}^a_{j,k} + \sum_{a,j}\sum_{b\neq a}\mathcal{D}^{a,b}_{j}, \tag{2}$$

where the labeling of the emitter, emittee (one emitted by the emitter), and spectator follows the convention in Refs. [14,36]. Summing over all contributing flavor combinations gives complete sets of dipoles for the quark (photon) induced processes, whose detailed forms are lengthy and will not be given here; they can be straightforwardly derived following the generic formulae for dipole terms in Refs. [35,42], with a similar notation as given in Appendix A of Ref. [14]. Note that the first term in Eq. (2) represents dipoles with both the splitting particles and the spectator from the final state. This type of dipoles is not present in the CC processes.

The contribution from 4-particle final states is then obtained by subtracting the singularities from the real emission cross section,

$$\sigma^{\rm NLO}_4 = \sum_b \int_0^1 d\eta_b f_b(\eta_b,\mu_F)\frac{1}{2\hat{s}}d\Phi_4 \times \left\{|\mathcal{M}^b_R|^2 F^{(2)}(p_1,p_2,p_3,p_4;P_A,p_b) - |\mathcal{M}^b_{\rm sub}|^2\right\}, \tag{3}$$

with a sum over the parton flavor b that collides with the incoming electron. A particular jet algorithm is implemented via the function $F^{(2)}$ as well as an implicit $F^{(1)}$ multiplied with the subtraction term in order to ensure IR and collinear safety for jet observables.[6]

2. 3-particle final states

The contribution of the 3-particle final states comes from loop-graph terms combined with integrated dipoles as well as collinear counter terms in a certain factorization scheme. After a reorganization of terms, one arrives at an expression,

$$\begin{aligned}\sigma^{\rm NLO}_3 = \sum_b \int d\eta_b f_b(\eta_b,\mu_F)\Bigg\{&\int \frac{1}{2\hat{s}}d\Phi^{(4)}_3\left[V_{ab}(\Phi_3,P_A,p_b) + B_{ab}(\Phi_3,P_A,p_b)\boldsymbol{I}^b(\epsilon,\mu^2)\right]_{\epsilon=0}\\ &+\sum_{a'}\int dx_a\int\frac{1}{2\hat{s}}d\Phi^{(4)}_3 B_{a'b}(\Phi^{(4)}_3,x_aP_A,p_b)\left[\boldsymbol{K}^b_{aa'}(x_a)+\boldsymbol{P}^b_{aa'}(x_a;\mu^2_F)\right]\\ &+\sum_{b'}\int dx_b\int\frac{1}{2\hat{s}}d\Phi^{(4)}_3 B_{ab'}(\Phi^{(4)}_3,P_A,x_bp_b)\left[\boldsymbol{K}^a_{bb'}(x_b)+\boldsymbol{P}^a_{bb'}(x_b;\mu^2_F)\right]\Bigg\}\\ &+\sum_b\int d\eta_a d\eta_b f^{\mathcal{O}(\alpha)}_e(\eta_a,\mu_F)f_b(\eta_b,\mu_F)\int\frac{1}{2\hat{s}}d\Phi^{(4)}_3 B_{ab}\left(\Phi^{(4)}_3,p_a,p_b\right).\end{aligned} \tag{4}$$

[6]One could also consider collinear unsafe observables [43]. Distributions in this case are enhanced logarithmically by final state radiations in collinear regions. For simplicity, however, this kind of observables is not explored in this study.

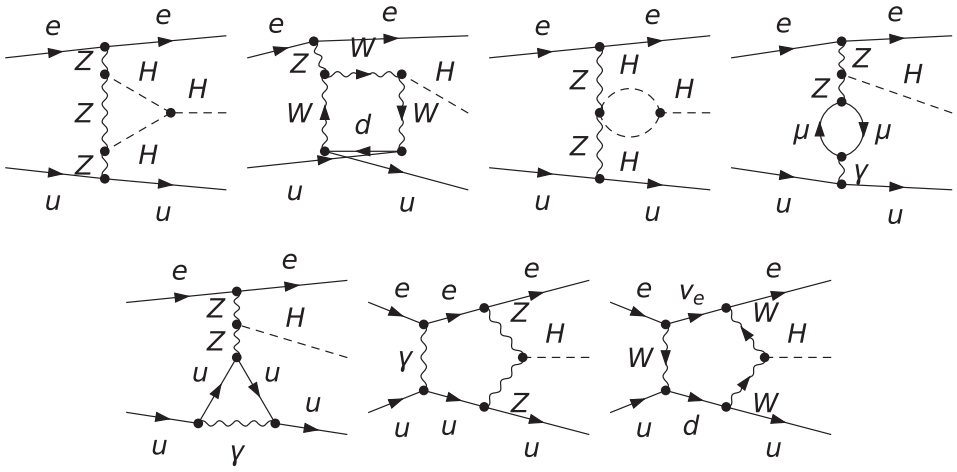

FIG. 3. Representative one-loop graphs for NC WBF at the LHeC.

The terms with V_{ab} is from one-loop graphs. In this calculation, 2280 one-loop graphs (see examples in Fig. 3) are produced and evaluated by the program Madgraph5_AMC@NLO [44]. Renormalization of parameters is done in both G_μ and $\alpha(M_Z)$ schemes [45,46]. Again, the explicit forms of the $\boldsymbol{I}$,$\boldsymbol{K}$, and $\boldsymbol{P}$ terms are taken and adapted to our processes from Refs. [35,42], and are not shown here. The last line of Eq. (4) is obtained by factorization of an electron distribution function to simplify the treatment of the initial state radiations, where the $\mathcal{O}(\alpha)$ electron distribution reads [47],

$$f_e^{\mathcal{O}(\alpha)}(x,\mu_F) = \frac{\alpha}{2\pi}\left[\frac{1+x^2}{1-x}\ln\frac{\mu_F^2}{(1-x)^2 m_e^2}\right]_+ . \tag{5}$$

The factorization of both the electron and partons from the proton is carried out in the $\overline{\text{MS}}$ scheme. A jet definition, as remarked at the end of Sec. II B 1, is applied to the 3-particle final states by an implicit function $F^{(1)}$ both at LO and NLO.

We want to stress that the $\boldsymbol{K}$ and $\boldsymbol{P}$ terms in Eq. (4) are arranged to carry the factorization scheme dependence of the collinear counter terms that are added to cancel the collinear divergences from the initial state radiations in the hard-scattering cross sections. From the factorization structure of these terms one could see that the second and fourth lines of Eq. (4) can be combined to remove the factorization scheme dependence (up to higher order terms). The same can be done by combining the third line of Eq. (4) with the LO cross section in Eq. (1), whereas the first line of Eq. (4) is independent of the factorization scheme by itself.

III. NUMERICAL RESULT

The beam energies and SM parameters for this calculation are taken as

$$\begin{aligned}
&E_e = 140\ \text{GeV}, \qquad E_p = 7\ \text{TeV},\\
&G_\mu = 1.16639\times 10^{-5}\ \text{GeV}^{-2}, \qquad \alpha_{G_\mu} = 1/132.5, \qquad \alpha(M_Z) = 1/128.93,\\
&M_W = 80.419\ \text{GeV}, \qquad \Gamma_W = 2.09291\ \text{GeV}, \qquad M_Z = 91.188\ \text{GeV},\\
&\Gamma_Z = 2.49877\ \text{GeV}, \qquad c_W^2 = 1 - s_W^2 = \frac{M_W^2}{M_Z^2},\\
&m_e = 0.510998928\ \text{MeV}, \qquad M_H = 125\ \text{GeV}.
\end{aligned} \tag{6}$$

A unit Cabibbo-Kobayashi-Maskawa matrix is used for simplicity, and we take M_W for the renormalization and factorization scales. All quark and electron masses are set to zero in the scattering amplitudes, which reduces substantially the number of graphs to be evaluated. The 3- and 4- particle phase spaces are generated in our own program that relies on the Vegas Monte Carlo algorithm from the CUBA library [48] for numerical integration.

The PDF set `CT18qed_proton` [49] is used in this calculation, in which the NLO QED evolution is implemented and the photon distribution is constrained with the LUX method [50,51] to achieve an order-of-magnitude improvement of accuracy as compared with earlier CTEQ photon PDFs. Checks of the calculation similar to those in the CC case are done until a consistent and stable result is obtained.

TABLE I. Integrated cross sections in fb for NC WBF at the LHeC at LO and NLO, computed in two renormalization schemes G_μ and $\alpha(M_Z)$. The electron and proton beam energies are 140 GeV and 7 TeV, respectively. The LO, 3-particle, and 4-particle contributions are respectively computed according to Eqs. (1), (4), and (3). Their sum gives the total cross section in the second column.

Schemes	Total	LO	3-particle	4-particle
G_μ	47.21	51.00	−3.88	0.09
$\alpha(M_Z)$	46.15	55.37	−9.32	0.10

Now we show our numerical results of cross sections computed with the setup above. The total integrated cross sections listed in Table I are about 20% of those in CC case. However, the corrections from the NLO terms relative to the LO ones are respectively −8% and −17% in G_μ and $\alpha(M_Z)$ schemes, which are very close to the results for CC processes. Furthermore, the decomposition of the total cross sections into various contributions at LO and NLO in two schemes shows a pattern of convergence very similar to the CC result, which reflects once again the renormalization scheme independence of the physical result. At NLO, the ratio between the contributions from 3- and 4-particle final states increases by a factor of 4 as compared with the CC case. This is rouphly proportional to the increase of the ratio between the number of loop- and real-graphs in NC WBF.

For differential distributions, we first construct quark jets and electron observables according to the k_T algorithm [52–54] with the parameter $D = 0.8$. Hence the electron observables we shall discuss below receive contribution from the photon momentum in the soft and collinear limits. Next, we apply selection cuts to the jet with the largest transverse momentum (tagging jet), as well as to the electron observables, requiring,

$$p_T^j > 30\ \text{GeV}, \qquad p_T^e > 25\ \text{GeV},$$
$$-5 < \eta_j, \eta_e < -5, \tag{7}$$

where these quantities are defined with respect to the forward direction in which the incoming electron is moving. Cuts on transverse momenta are inherited from the CC calculation to maintain a typical event shape of WBF. The requirement on rapidities is loosened as compared with the CC case, because the NC signal is much smaller at the LHeC and could not afford a substantial loss. For the same reason we no longer restrict the invant mass of the Higgs-tagging jet (or of the Higgs-electron) system [8].

To present the result, we compare various cross sections computed to LO and NLO (LO + NLO corrections). We shall work in the G_μ scheme as it leads to a faster convergence of the perturbative calculation. Figure 4 shows the transverse momentum distribution and the corresponding K factors of the tagging jet. The curves on the left drop rapidly at large p_T^j, and the NLO correction is negative throughout the entire spectrum shown. The p_T^j of a typical event is located around $\mathcal{O}(M_Z)$, as is expected for the WBF. The K factor plot on the right shows the distribution computed up to NLO divided by the corresponding one at LO. Also displayed are the K factors with solely the loop contribution and with solely the initial state radiations (ISR) off the electron [i.e., the contribution from the $\mathcal{O}(\alpha)$ electron distribution function], respectively, at NLO. According to the discussion about the factorization scheme dependence of various terms at the end of Sec. II B 2, the loop contribution is computed using the first line of Eq. (4), and the ISR contribution is computed by combining the second and fourth lines. Corrections from both sources are about −5% and change slowly with increasing p_T^j. However, their sum gives almost a constant K factor ∼0.93, as can be seen from the blue curve. Note that the NLO

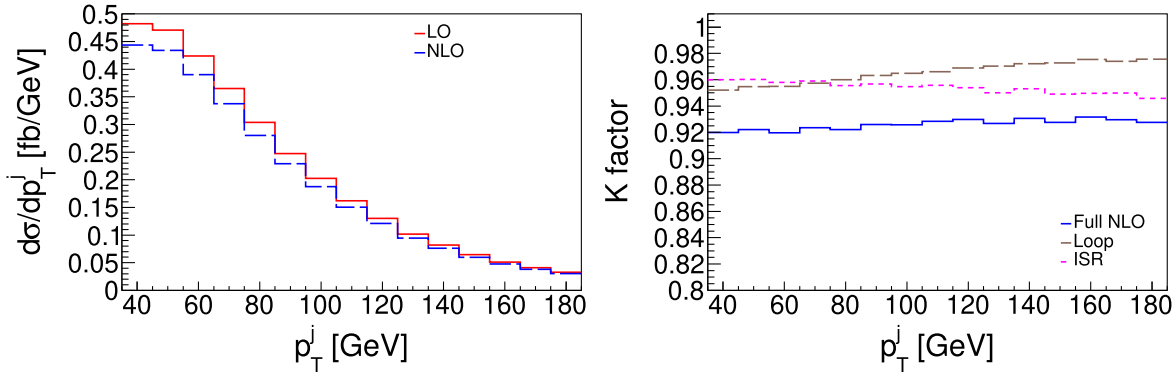

(a) p_T^j distribution (b) K factor

FIG. 4. Distribution in the transverse momentum p_T^j of the tagging jet (a), and the corresponding K factors (b).

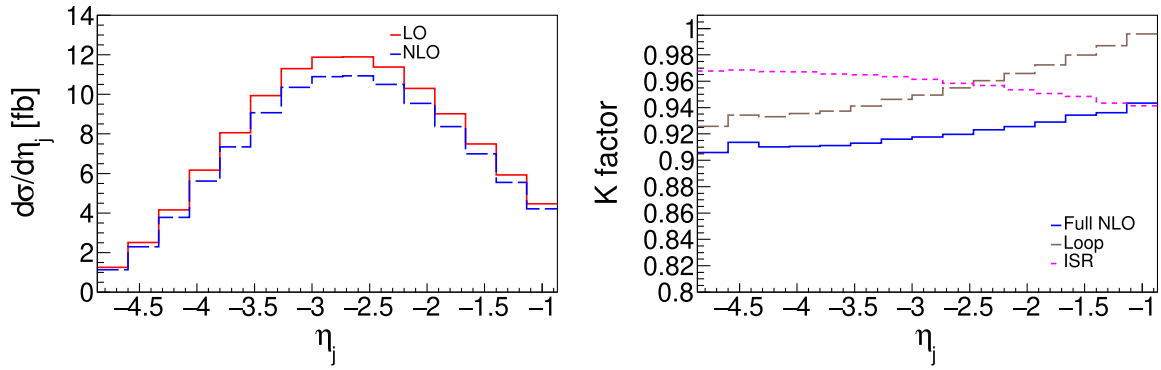

(a) η_j distribution (b) K factor

FIG. 5. Distribution in the rapidity η_j of the tagging jet (a), and the corresponding K factors (b).

corrections include contributions from all lines of Eq. (4) as well as from Eq. (3). However, the relative corrections from the 4-particle final states and from the $\boldsymbol{K}$ and $\boldsymbol{P}$ terms in Eq. (4) are within 0.3% and 1%, respectively, over the ranges of p_T^j and of all other observables to be explored below. We therefore do not separately show these corrections, and the blue curve is essentially given by the contributions of loop and ISR terms.

The tagging jet rapidity in Fig. 5 covers mostly the backward region and peaks around $\eta_j = -3$. The relative corrections at NLO are still rather stable (∼7%) for different η_j, even though the K factors of loop and ISR contributions vary slowly in opposite trends as η_j changes.

In searchings of Higgs invisible decays, it is important to make use of the electron observables together with those of the tagging jet. This proves to be useful in suppressing the background $p + e^- \to W^-(\to e^-\bar{\nu}_e) + j + \nu_e$ at the LHeC [34]. The distribution of p_T^e in Fig. 6 behaves very similarly to that of p_T^j, both at LO and NLO, as is expected from the characteristics of WBF events. In contrast, the electron and tagging jet rapidities are very different. The outgoing electron tends to be in the forward region with a more concentrated distribution of η_e (as compared with η_j) around 1 [see Fig. 7(a)]. Furthermore, the NLO corrections in Fig. 7(b) become positive and sizeable (as large as 35%) in going to the negative η_e, despite that the cross sections in this region die out. It is interesting to observe that both the loop and ISR corrections at NLO are positive in this region. While the loop terms are very complicated to analyze, it is fairly straightforward to explain the behavior of the ISR corrections. The negative corrections from the virtual ISR become more important when the c.m. energy of the beams is near the threshold of producing the hard-scattering final state [55,56]. The K factor of the ISR above 1 in the negative η_e region, however, suggests the converse scenario where the c.m. energy of the beams is much larger than the threshold of the hard-scattering final state. This allows for a large phase space for the positive contribution from the real photon radiations off the initial electron that may compensate the negative corrections of the virtual ISR. The net NLO corrections at large and positive η_e reaches −15%. Over the entire spectrum of η_e, the variation of loop corrections is milder than the ISR.

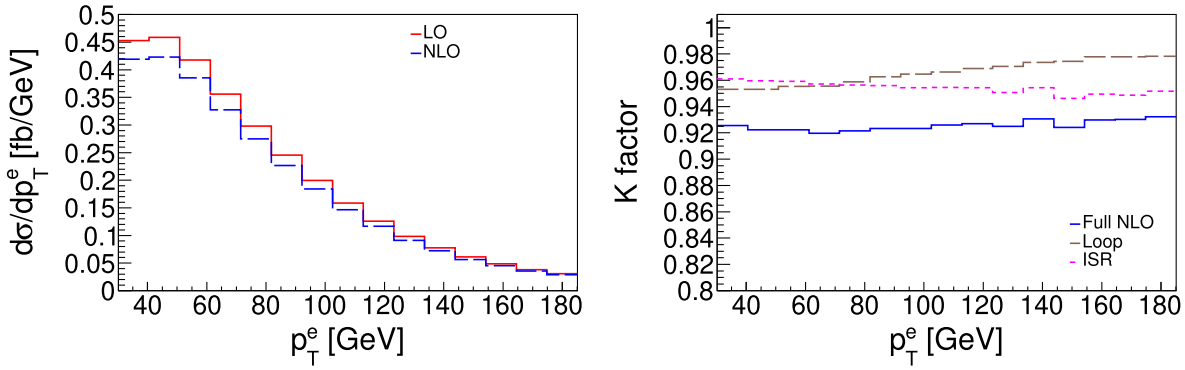

(a) p_T^e distribution (b) K factor

FIG. 6. Distribution in the transverse momentum p_T^e of the outgoing electron (a), and the corresponding K factors (b).

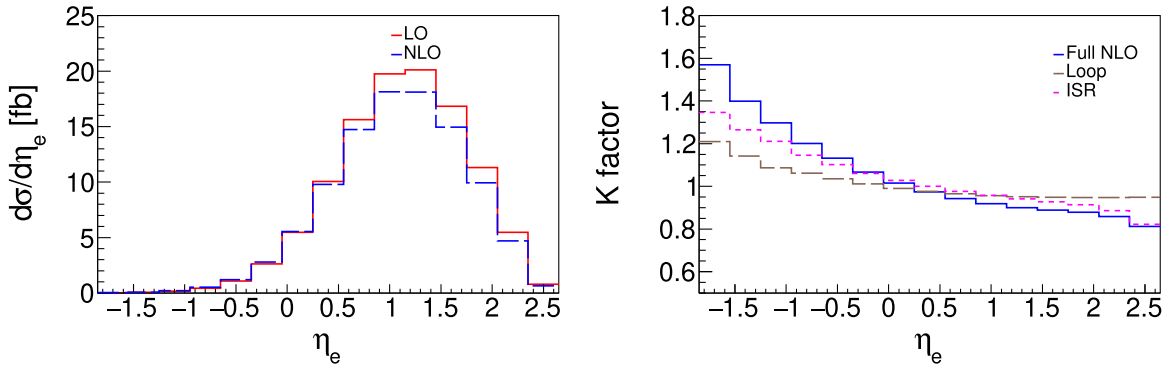

(a) η_e distribution (b) K factor

FIG. 7. Distribution in the rapidity η_e of the outgoing electron (a), and the corresponding K factors (b).

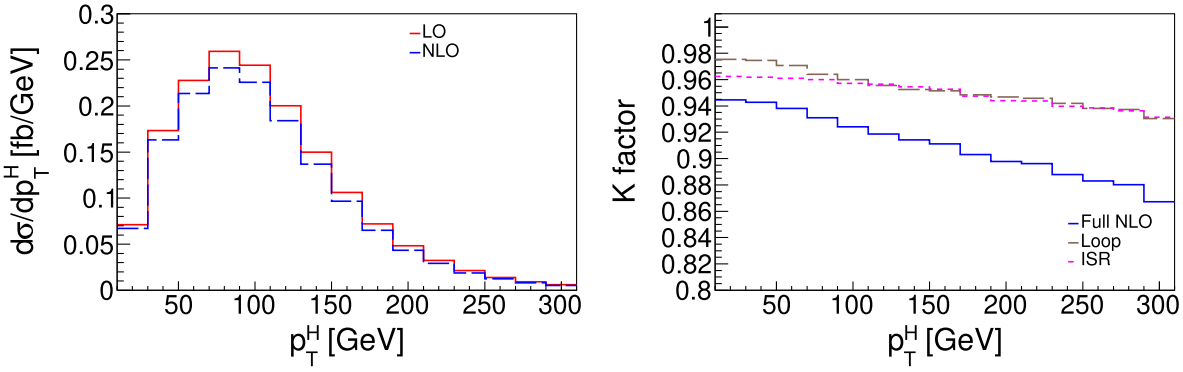

(a) p_T^H distribution (b) K factor

FIG. 8. Distribution in the transverse momentum p_T^H of the Higgs boson (a), and the corresponding K factors (b).

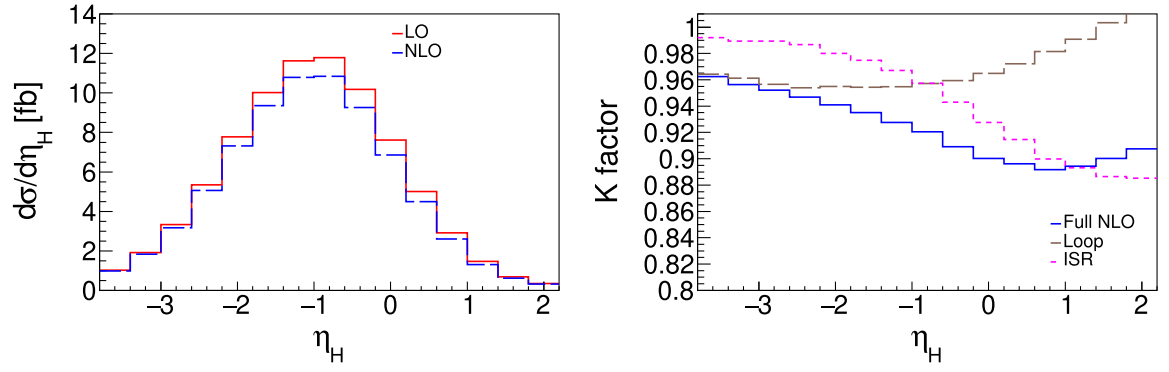

(a) η_H distribution (b) K factor

FIG. 9. Distribution in the rapidity η_H of the Higgs boson (a), and the corresponding K factors (b).

The typical transverse momentum of the Higgs is much larger than those of the final state fermions. Figure 8 shows that p_T^H peaks at 100 GeV and extends over 300 GeV. The relative corrections at NLO changes between -5% to -13% in this range, where the loop and ISR terms give comparable contributions. The η_H distribution in Fig. 9 centers near -1 and appears fairly symmetric on the two sides. Within the range $-4 < \eta_H < 2$, the NLO K factor varies between 0.97 to 0.9, and essentially interpolates between the curves of the loop terms and of the ISR. The

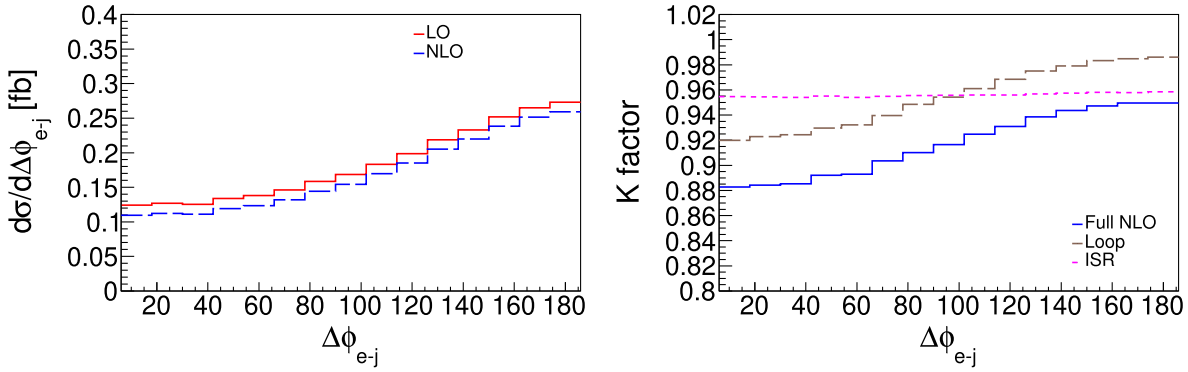

(a) $\Delta\phi_{e-j}$ distribution (b) K factor

FIG. 10. Distribution in the azimuthal angle difference between the tagging jet and the outgoing electron (a), and the corresponding K factors (b).

decrease of the ISR K factor at large p_T^H and positive η_H is consistent with the fact that these regions are typically reached by a large collision energy.

The last observable we shall explore is the azimuthal angle difference between the tagging jet and the final-state electron. This quantity has been shown to be sensitive to Higgs anomalous couplings with gauge bosons, and are used to distinguish these couplings from the SM ones [57–59]. As with the CC case, the distribution of $\Delta\phi_{e-j}$ in Fig. 10 is going through a steady and monotonic increase within the range $\Delta\phi_{e-j} \in [0, \pi]$. The K factor increases within the same range from 0.9 to 0.95, with the trend dominated by loop corrections. The ISR terms are not sensitive to the change of $\Delta\phi_{e-j}$ and contribute roughly a constant relative correction about -4%. It is worth mentioning that the azimuthal angle difference is an effective observable to reduce backgrounds for WBF production of invisible Higgs bosons at both the LHC [21] and LHeC [34]. These searches require the azimuthal angle difference to be less than about 70°, which is in Fig. 10(b) just the region where the NLO corrections are most pronounced.

IV. CONCLUSION

In this work we have computed the NLO EW effects for the NC WBF processes at the LHeC. The dipole subtraction formalism is adopted for organizing various singularities encountered at one-loop order. A factorization of the electron distribution is done in order to simplify the electron mass dependence in the hard-scattering cross sections. The numerical result of the calculation is obtained in both G_μ and $\alpha(M_Z)$ renormalization schemes for the c.m. energy of the electron-proton beams at 1.98 TeV. While the sizes of the NLO terms computed in the two schemes differ by $\sim 50\%$, the results of LO + NLO in two schemes agree up to higher order corrections. The G_μ scheme leads to a faster convergence of the perturbative calculation, and is used for computing several differential distributions. In the spectra of the considered observables where most contributing events reside, the corrections are negative and within the range $[-13\%, 0]$. The only large positive corrections are observed in the region where the rapidity of the final-state electron becomes negative, i.e., as it recoils against the proton beam. The Higgs observables are more sensitive to the EW radiative effects. The roles of the ISR and loop terms are quite different in distorting the LO distributions, despite that they both give sizable corrections. Overall, the NLO corrections are at the level of 10% and are significant in modifying both the normalization and shape of the LO distributions; they should be included in a full phenomenological analysis of the NC WBF production of the Higgs at the LHeC.

ACKNOWLEDGMENTS

This work was supported by National Natural Science Foundation of China (12105068). B. W. and H. X. were also supported by Hangzhou Normal University Start-up Funds.

[1] G. Aad *et al.* (ATLAS Collaboration), Observation of a new particle in the search for the Standard Model Higgs boson with the ATLAS detector at the LHC, Phys. Lett. B **716**, 1 (2012).

[2] S. Chatrchyan *et al.* (CMS Collaboration), Observation of a new boson at a mass of 125 GeV with the CMS experiment at the LHC, Phys. Lett. B **716**, 30 (2012).

[3] ATLAS Collaboration, A combination of measurements of Higgs boson production and decay using up to 139 fb^{-1} of proton–proton collision data at $\sqrt{s} = 13$ TeV collected with the ATLAS experiment.

[4] CMS Collaboration, Combined Higgs boson production and decay measurements with up to 137 fb^{-1} of proton-proton collision data at $\sqrt{s} = 13$ TeV.

[5] A. M. Sirunyan *et al.* (CMS Collaboration), Observation of the Higgs boson decay to a pair of τ leptons with the CMS detector, Phys. Lett. B **779**, 283 (2018).

[6] M. Aaboud *et al.* (ATLAS Collaboration), Cross-section measurements of the Higgs boson decaying into a pair of τ-leptons in proton-proton collisions at $\sqrt{s} = 13$ TeV with the ATLAS detector, Phys. Rev. D **99**, 072001 (2019).

[7] J. L. Abelleira Fernandez *et al.* (LHeC Study Group), A large hadron electron collider at CERN: Report on the physics and design concepts for machine and detector, J. Phys. G **39**, 075001 (2012).

[8] T. Han and B. Mellado, Higgs boson searches and the H b anti-b coupling at the LHeC, Phys. Rev. D **82**, 016009 (2010).

[9] P. Agostini *et al.* (LHeC, FCC-he Study Group Collaborations), The large hadron-electron collider at the HL-LHC, J. Phys. G **48**, 110501 (2021).

[10] R. Li, B.-W. Wang, K. Wang, X. Zhang, and Z. Zhou, Probing the charm Yukawa coupling at future $e^- p$ and $e^+ e^-$ colliders, Phys. Rev. D **100**, 053008 (2019).

[11] R. Li, X.-M. Shen, B.-W. Wang, K. Wang, and G. Zhu, Probing the trilinear Higgs boson self-coupling via single Higgs production at the LHeC, Phys. Rev. D **101**, 075036 (2020).

[12] B. Jager, Next-to-leading order QCD corrections to Higgs production at a future lepton-proton collider, Phys. Rev. D **81**, 054018 (2010).

[13] J. Blumlein, G. J. van Oldenborgh, and R. Ruckl, QCD and QED corrections to Higgs boson production in charged current e p scattering, Nucl. Phys. **B395**, 35 (1993).

[14] B. Wang, K. Wang, and H. Xiong, Electroweak corrections to Higgs boson production via W W fusion at the future LHeC, Phys. Rev. D **106**, 093011 (2022).

[15] Y. Bai, P. Draper, and J. Shelton, Measuring the invisible Higgs width at the 7 and 8 TeV LHC, J. High Energy Phys. 07 (2012) 192.

[16] D. Ghosh, R. Godbole, M. Guchait, K. Mohan, and D. Sengupta, Looking for an invisible Higgs signal at the LHC, Phys. Lett. B **725**, 344 (2013).

[17] B. Dutta, A. Gurrola, W. Johns, T. Kamon, P. Sheldon, and K. Sinha, Vector boson fusion processes as a probe of supersymmetric electroweak sectors at the LHC, Phys. Rev. D **87**, 035029 (2013).

[18] A. G. Delannoy *et al.*, Probing dark matter at the LHC using vector boson fusion processes, Phys. Rev. Lett. **111**, 061801 (2013).

[19] C. Bernaciak, T. Plehn, P. Schichtel, and J. Tattersall, Spying an invisible Higgs boson, Phys. Rev. D **91**, 035024 (2015).

[20] N. Arkani-Hamed, S. Dimopoulos, G. R. Dvali, and J. March-Russell, Neutrino masses from large extra dimensions, Phys. Rev. D **65**, 024032 (2001).

[21] O. J. P. Eboli and D. Zeppenfeld, Observing an invisible Higgs boson, Phys. Lett. B **495**, 147 (2000).

[22] A. Djouadi, O. Lebedev, Y. Mambrini, and J. Quevillon, Implications of LHC searches for Higgs–portal dark matter, Phys. Lett. B **709**, 65 (2012).

[23] C. Englert, T. Plehn, D. Zerwas, and P. M. Zerwas, Exploring the Higgs portal, Phys. Lett. B **703**, 298 (2011).

[24] Y. Mambrini, Higgs searches and singlet scalar dark matter: Combined constraints from XENON 100 and the LHC, Phys. Rev. D **84**, 115017 (2011).

[25] S. Baek, P. Ko, W.-I. Park, and E. Senaha, Higgs portal vector dark matter: Revisited, J. High Energy Phys. 05 (2013) 036.

[26] G. Belanger, B. Dumont, U. Ellwanger, J. F. Gunion, and S. Kraml, Status of invisible Higgs decays, Phys. Lett. B **723**, 340 (2013).

[27] D. Curtin *et al.*, Exotic decays of the 125 GeV Higgs boson, Phys. Rev. D **90**, 075004 (2014).

[28] M. Aaboud *et al.* (ATLAS Collaboration), Combination of searches for invisible Higgs boson decays with the ATLAS experiment, Phys. Rev. Lett. **122**, 231801 (2019).

[29] V. Khachatryan *et al.* (CMS Collaboration), Searches for invisible decays of the Higgs boson in pp collisions at $\sqrt{s} = 7$, 8, and 13 TeV, J. High Energy Phys. 02 (2017) 135.

[30] A. Tumasyan *et al.* (CMS Collaboration), Search for invisible decays of the Higgs boson produced via vector boson fusion in proton-proton collisions at $s = 13$ TeV, Phys. Rev. D **105**, 092007 (2022).

[31] A. M. Sirunyan *et al.* (CMS Collaboration), Search for invisible decays of a Higgs boson produced through vector boson fusion in proton-proton collisions at $\sqrt{s} = 13$ TeV, Phys. Lett. B **793**, 520 (2019).

[32] G. Aad *et al.* (ATLAS Collaboration), Search for invisible decays of a Higgs boson using vector-boson fusion in pp collisions at $\sqrt{s} = 8$ TeV with the ATLAS detector, J. High Energy Phys. 01 (2016) 172.

[33] G. Aad *et al.* (ATLAS Collaboration), Observation of electroweak production of two jets in association with an isolated photon and missing transverse momentum, and search for a Higgs boson decaying into invisible particles at 13 TeV with the ATLAS detector, Eur. Phys. J. C **82**, 105 (2022).

[34] Y.-L. Tang, C. Zhang, and S.-h. Zhu, Invisible Higgs Decay at the LHeC, Phys. Rev. D **94**, 011702 (2016).

[35] S. Catani and M. H. Seymour, A General algorithm for calculating jet cross-sections in NLO QCD, Nucl. Phys. **B485**, 291 (1997); Nucl. Phys. **B510**, 503(E) (1998).

[36] M. Schönherr, An automated subtraction of NLO EW infrared divergences, Eur. Phys. J. C **78**, 119 (2018).

[37] T. Hahn, Generating Feynman diagrams and amplitudes with FeynArts 3, Comput. Phys. Commun. **140**, 418 (2001).

[38] T. Hahn and M. Perez-Victoria, Automatized one loop calculations in four-dimensions and D-dimensions, Comput. Phys. Commun. **118**, 153 (1999).

[39] A. Denner, S. Dittmaier, M. Roth, and D. Wackeroth, Predictions for all processes $e^+e^- \to 4$ fermions + gamma, Nucl. Phys. **B560**, 33 (1999).
[40] A. Denner, S. Dittmaier, M. Roth, and L. H. Wieders, Electroweak corrections to charged-current $e^+e^- \to 4$ fermion processes: Technical details and further results, Nucl. Phys. **B724**, 247 (2005); Nucl. Phys. **B854**, 504(E) (2012).
[41] A. Denner and S. Dittmaier, The complex-mass scheme for perturbative calculations with unstable particles, Nucl. Phys. B, Proc. Suppl. **160**, 22 (2006).
[42] S. Catani, S. Dittmaier, M. H. Seymour, and Z. Trocsanyi, The dipole formalism for next-to-leading order QCD calculations with massive partons, Nucl. Phys. **B627**, 189 (2002).
[43] S. Dittmaier, A. Kabelschacht, and T. Kasprzik, Polarized QED splittings of massive fermions and dipole subtraction for non-collinear-safe observables, Nucl. Phys. **B800**, 146 (2008).
[44] J. Alwall, R. Frederix, S. Frixione, V. Hirschi, F. Maltoni, O. Mattelaer, H. S. Shao, T. Stelzer, P. Torrielli, and M. Zaro, The automated computation of tree-level and next-to-leading order differential cross sections, and their matching to parton shower simulations, J. High Energy Phys. 07 (2014) 079.
[45] A. Denner, Techniques for calculation of electroweak radiative corrections at the one loop level and results for W physics at LEP-200, Fortschr. Phys. **41**, 307 (1993).
[46] A. Denner and S. Dittmaier, Electroweak radiative corrections for collider physics, Phys. Rep. **864**, 1 (2020).
[47] T. Liu, W. Melnitchouk, J.-W. Qiu, and N. Sato, A new approach to semi-inclusive deep-inelastic scattering with QED and QCD factorization, J. High Energy Phys. 11 (2021) 157.
[48] T. Hahn, CUBA: A library for multidimensional numerical integration, Comput. Phys. Commun. **168**, 78 (2005).
[49] K. Xie, T. J. Hobbs, T.-J. Hou, C. Schmidt, M. Yan, and C. P. Yuan (CTEQ-TEA Collaboration), Photon PDF within the CT18 global analysis, Phys. Rev. D **105**, 054006 (2022).
[50] A. Manohar, P. Nason, G. P. Salam, and G. Zanderighi, How bright is the proton? A precise determination of the photon parton distribution function, Phys. Rev. Lett. **117**, 242002 (2016).
[51] A. V. Manohar, P. Nason, G. P. Salam, and G. Zanderighi, The photon content of the proton, J. High Energy Phys. 12 (2017) 046.
[52] S. Catani, Y. L. Dokshitzer, and B. R. Webber, The K^- perpendicular clustering algorithm for jets in deep inelastic scattering and hadron collisions, Phys. Lett. B **285**, 291 (1992).
[53] S. D. Ellis and D. E. Soper, Successive combination jet algor-ithm for hadron collisions, Phys. Rev. D **48**, 3160 (1993).
[54] G. C. Blazey *et al.*, Run II jet physics, in *Physics at Run II: QCD and Weak Boson Physics Workshop: Final General Meeting* (2000), pp. 47–77, arXiv:hep-ex/0005012.
[55] A. Denner, S. Dittmaier, M. Roth, and M. M. Weber, Electroweak radiative corrections to $e^+e^- \to t\bar{t}$H, Phys. Lett. B **575**, 290 (2003).
[56] A. Denner, S. Dittmaier, M. Roth, and M. M. Weber, Electroweak corrections to $e^+e^- \to$ f anti-f H, Nucl. Phys. B, Proc. Suppl. **135**, 88 (2004).
[57] T. Plehn, D. L. Rainwater, and D. Zeppenfeld, Determining the structure of Higgs couplings at the LHC, Phys. Rev. Lett. **88**, 051801 (2002).
[58] S. S. Biswal, R. M. Godbole, B. Mellado, and S. Raychaudhuri, Azimuthal angle probe of anomalous HWW couplings at a high energy ep collider, Phys. Rev. Lett. **109**, 261801 (2012).
[59] P. Sharma and A. Shivaji, Probing non-standard HVV (V = W, Z) couplings in single Higgs production at future electron-proton collider, J. High Energy Phys. 10 (2022) 108.

Correction: The omission of the "Contact author" label in the footnote for the last author has been fixed.